Solar-Terrestrial Physics. 2026, vol. 12, iss. 2, pp. 57–68. DOI: 10.12737/stp-122202607. © 2026 A.A. Budovkina et al. Published by INFRA-M Academic Publishing House

DOI: 10.12737/stp-122202607
EDN: GCJSGS

Received September 01, 2025
Accepted November 27, 2025

SEASONAL VARIABILITY OF HORIZONTAL NEUTRAL WIND IN THE BAIKAL REGION FROM FABRY — PEROT INTERFEROMETER OBSERVATIONS AND DIFFERENT VERSIONS OF HWM

A.A. Budovkina
Institute of Solar Terrestrial Physics SB RAS, Irkutsk, Russia, abudovkina@iszf.irk.ru

I.K. Edemskiy
Institute of Solar Terrestrial Physics SB RAS, Irkutsk, Russia, ilya@iszf.irk.ru

R.V. Vasilyev
Institute of Solar Terrestrial Physics SB RAS, Irkutsk, Russia, roman_vasilyev@iszf.irk.ru

M.F. Artamonov
Institute of Solar Terrestrial Physics SB RAS, Irkutsk, Russia, artamonov.maksim@iszf.irk.ru

Abstract. This study is based on observations of the atomic oxygen airglow emission at 630 nm obtained with a Fabry—Perot interferometer (FPI) of the National Heliogeophysical Complex. FPI is installed in the Geophysical Observatory of the Institute of Solar-Terrestrial Physics SB RAS (Tory, 52° N, 103° E). Doppler shifts of the emission line were measured and then converted into horizontal wind velocities along the zonal and meridional directions during nighttime and twilight periods. We analyze the seasonal variability of neutral wind components during 2022, using both FPI measurements and model calculations from three versions of the Horizontal Wind Model: HWM93, HWM07, and HWM14. The analysis covers local nighttime hours (10–24 UTC). The data was separated by seasons relative to solstices and equinoxes and filtered by cloud conditions.

The discrepancies between modeled and observed wind components vary with both local time and season. None of the HWM versions provide acceptable agreement with the measurements, indicating that HWM outputs for the Baikal region should not be considered accurate. The results of this study can be used to develop recommendations for improving or adjusting HWM in order to better describe the dynamics of the upper atmosphere in the region. These findings are also useful when choosing the most suitable HWM version for estimating a specific wind component in a given season.

Keywords: Horizontal Wind Model (HWM), Fabry—Perot interferometer, neutral wind, thermosphere.

INTRODUCTION

The height profile of the neutral wind in the atmosphere is determined primarily by temperature gradients formed by solar radiation, which create a pressure difference between the day and night sides of Earth, as well as between low and high latitudes [Matveev, 1984]. The Coriolis force, which prevails in the troposphere and stratosphere, forms jet streams and trade winds, but its effect weakens above 100 km due to a decrease in air density and an increase in the dominant role of ion-neutral interaction [Holton, Hakim, 2012; Richmond, Maute, 2014]. Tidal and internal gravity waves (IGWs) generated in the lower atmosphere (for example, by convection in the troposphere or orographic disturbances) transfer energy and momentum to the upper layers. The amplitude of IGWs increases exponentially with altitude due to a decrease in density, which leads to their destruction in the mesosphere and thermosphere, where they transfer part of their energy to heating of the medium; and the remaining momentum, to the neutral wind [Matveev, 1984].

At ionospheric heights (above 100 km), the ion-neutral collision influence becomes significant. As a result, configurations of the electric field and currents largely depend on neutral wind parameters [Richmond, Maute, 2014]. The amplification of ionospheric currents during geomagnetic storms and substorms through interaction with neutral particles causes an increase in winds in the polar thermosphere to 500–1000 m/s, which affects wind dynamics on a global scale [Prölss, 2012].

It can be said that due to the presence of nonlinearities of the interaction, processes of various nature, and effects of different forces, as well as seasonal, latitudinal, and geomagnetic dependences of individual components of the processes, the problem of predicting the neutral wind magnitude is extremely difficult. The situation is complicated by the limited observational database, especially at ionospheric heights, where it is impossible to use meteorological balloons, and remote lidar and radar techniques are effective only in the lower ionosphere (resonant scattering by metal ions and meteor trail radiolocation). The dynamics of the upper ionosphere can be successfully observed with ionosondes and incoherent scatter radars, yet its relationship with the neutral wind is ambiguous owing to the presence of plasma-chemical and other factors in addition to wind dynamics, which affect plasma concentration variability. Satellite measurements are irregular and do not al-

low us to study the diurnal variation of the wind with high time resolution.

Meanwhile, there are various models that are extensively employed to calculate neutral wind components: TIE-GCM (Thermosphere — Ionosphere Electrodynamics General Circulation Model) [Richmond et al., 1992], GITM (Global Ionosphere Thermosphere Model) [Ridley et al., 2006], CTIM (Coupled Thermosphere — Ionosphere Model) [Fuller-Rowell et al., 1996], GSM-TIP [Klimenko et al., 2007]. Particular emphasis should be placed upon the Horizontal Wind Model (HWM). It is based on empirical information about the neutral wind collected from various sources (ionosondes, satellite experiments, ground-based Fabry — Perot interferometers, etc.). In this study, we present the neutral wind components obtained from ground-based optical observations within a year and compare them with the model values from HWM of three up-to-date versions. Similar studies of the neutral wind with ground-based Fabry — Perot interferometers were carried out at midlatitudes of China [Yao et al., 2015; Yang et al., 2020] and in East Asia when compared with global models [Jiang et al., 2018], as well as at high latitudes in Norway [Xu et al., 2019]. These works showed stable seasonal and intradiurnal patterns, as well as systematic discrepancies depending on latitude, season, and solar activity level, modeled with HWM and observed values [Emmert et al., 2006; Okoh et al., 2022]. This paper supplements the picture with unique data for the Baikal region (midlatitude Eurasia) and evaluates the agreement between observations with the 630 nm Fabry—Perot interferometer and HWM of various versions in 2022.

The aim of this paper is to determine the version (or combination of versions) of the model, which gives the best fit to observations.

1. DATA ANALYSIS AND COMPARISON

1.1. Horizontal wind model

HWM is an empirical model describing the horizontal neutral wind. It is based on data collected from both satellites and ground-based instruments, including radars and Fabry — Perot interferometers [https://ccmc.gsfc.nasa.gov/models/HWM14~2014]. There are five versions of this model, differing in the set of initial data and the range of altitudes to which the forecast applies (Table 1).

The first version of the model called HWM87 was used to predict winds at altitudes above 220 km [Hedin et al., 1988]. Later, in 1990, an advanced version of the model, HWM90, appeared. It included wind data obtained by ground-based instruments: incoherent scatter radars and optical Fabry — Perot interferometers (FPI).

Table 1

Comparison between HWM versions

Version	Data sources	Altitudes
HWM87	AE-E and DE 2 satellites	from 220 to ~500 km
HWM90	AE-E and DE 2 satellites Ground-based incoherent scatter radars and optical Fabry — Perot interferometers	from 100 to ~500 km
HWM93	AE-E and DE 2 satellites Ground-based incoherent scatter radars and optical Fabry — Perot interferometers MF/Meteor radars	from ground level to 500 km
HWM07	AE-E and DE 2 satellites Ground-based incoherent scatter radars and optical Fabry — Perot interferometers MF/Meteor radars Height profiles from NASA/UARS-WINDII and -HRDI instruments	from ground level to 500 km
HWM14	AE-E and DE 2 satellites Ground-based incoherent scatter radars and optical Fabry — Perot interferometers MF/Meteor radars Height profiles from NASA/UARS-WINDII and -HRDI instruments Fabry — Perot interferometers at a wavelength of 630 nm in equatorial and polar regions Cross-track winds obtained from the Gravity Field and Steady State Ocean Circulation Explorer (GOCE) satellite (at ~250 km)	from ground level to 500 km

This model was employed to predict winds at altitudes of 100 km and above [Hedin et al., 1991]. In the HWM93 version, the model was expanded due to MF/Meteor radar data, which made it possible to predict winds from the ground level [Hedin et al., 1996]. HWM07 increases the capabilities of HWM93, as it is based on new observational data including the height profiles collected by NASA/UARS-WINDII and HRDI instruments [Drob et al., 2008]. The latest version of the model, HWM14, uses ground-based measurement data obtained by Fabry — Perot interferometers at a wavelength of 630 nm in equatorial and polar regions. When developed, this model was also supplemented with data, collected by the Gravity Field and Steady State Ocean Circulation Explorer (GOCE), on cross-track winds at an orbit altitude of ~250 km. In

addition, HWM07 [Drob et al., 2008] and HWM14 [Drob et al., 2015] provide two modes for the thermosphere: for quiet time and geomagnetically disturbed time.

In this paper, we use the Pyglow library to work with the model, which gives access to various atmospheric models such as HWM, IRI, and MSIS [https://github.com/timduly4/pyglow]. The library includes three most popular versions of HWM: HWM93, HWM07, and HWM14, written in Fortran. For convenience, there is a special Python warp that simplifies working with models. Moreover, the library allows us to run the model with up-to-date geospace indices. According to the HWM coordinate system, the zonal-wind component is considered positive when it is eastward; and the meridional-wind one, when it is northward.

1.2. Identification of wind components by the Fabry — Perot interferometer

Our paper is based on data from the Fabry—Perot interferometer installed at the Geophysical Observatory (GPhO) of the Institute of Solar-Terrestrial Physics of the Siberian Branch of the Russian Academy of Sciences (ISTP SB RAS). The observatory is located in Tory village (52° N, 103° E). Several such interferometers were purchased from KEO Scientific to create the first research facility "Optical Instruments" [Vasiliev et al., 2020] of the National Heliogeophysical Complex of the Russian Academy of Sciences (NHC RAS) [Zherebtsov, 2020].

The interferometer records the atomic oxygen emission O(^{1}D) at 630 nm. The most significant contribution to this emission and its variability is made by plasma-chemical reactions and dynamic atmospheric processes occurring at altitudes from 200 to 400 km [Vasiliev et al., 2017]. The work used wind speeds (zonal and meridional components) obtained from data on airglow characteristics measured by the interferometer. The accuracy of wind measurements with NHC RAS interferometers, as stated by the manufacturer, is 5–10 m/s.

The wind speed is determined from the Doppler shift of the emission wavelength caused by the collective motion of luminous air masses [Vasiliev et al., 2017]. For this purpose, four interference patterns are detected in a narrow (2.54°) field of view when observed in the cardinal directions (north, south, west, east) with 45° zenith angles. A shift of the wavelength of the detected emission relative to 630 nm is obtained from each interferogram. At given zenith and azimuth angles, we can find components of horizontal-wind projections onto the line of sight. If we assume that during these measurements the wind field above the observatory was uniform both in space and in time and the residual variations in the parameters also did not change, the horizontal wind velocity vector can be obtained through simple calculations:

$$V_i = c - c\left(\frac{\lambda_0 + \delta\lambda_i}{\lambda_0}\right),$$

where V_i is the velocity along the direction; c is the speed of light; λ_0 is the unshifted wavelength of emission (630 nm); $\delta\lambda_0$ is the Doppler shift observed in one of the cardinal directions. The i index indicates observations in northerly, southerly, easterly, and westerly directions (n, s, e, and w, respectively).

The zonal wind speed is calculated from the velocity values obtained in westerly and easterly directions with regard to the zenith angle of observations α=45°. At the same time, the effect of the vertical wind and the systematic errors having the same sign are reduced, and the zonal velocity projections onto the line of sight having different signs are added:

$$u = \frac{V_e - V_w}{2\cos\alpha}.$$

Similarly, from the data obtained in northerly and southerly directions we can find the meridional wind speed v:

$$v = \frac{V_n - V_s}{2\cos\alpha}.$$

These formulas allow us to estimate horizontal wind speeds from direct observation of the emission from small thermospheric regions (~10 km at an altitude 200–400 km) located in different directions. However, the light coming from the thermosphere passes through the troposphere and can be scattered by clouds and aerosols. Due to the nonuniform cloud density, the interferometer will detect a mixture of optical signals coming from different directions and having different Doppler shifts instead of optical radiation of one Doppler shift from a specific small region of the thermosphere. Under such conditions, the calculation of horizontal velocities from the formulas described above yields inaccurate results. Therefore, for a more correct calculation, observation conditions should be taken into account which can be determined from the number of stars in the all-sky camera field of view [Podlesnyi et al., 2022]. This criterion allows us to select data acquired under minimum cloud cover and/or aerosol density. Further in the paper, we divide measurements according to this criterion into several datasets: all measurements, clear-sky measurements, and cloudy-sky measurements.

1.3. Measurement data

In this paper, we use experimental data on the zonal and meridional wind speed components for one year (November 2021 – November 2022) obtained at night (local night from 10 to 24 UT). This time interval may vary slightly from season to season, as it depends on duration of night, but is generally within the specified limits.

For a more accurate calculation, during processing the data was separated into two categories: one included measurements corresponding to the entered condition "cloudy"; the other, "clear" (see the end of Subsection 1.2). For a given season, median values for each 15-min interval and the corresponding standard deviation (SD) were found. Seasons were determined from solstices and equinoxes. As a result, winter covers the period from November 7, 2021 to February 6, 2022 inclusive; spring, from February 7 to May 8, 2022; summer, from

May 9 to August 7, 2022; and autumn, from August 8 to November 6, 2022.

Figure 1 illustrates the median zonal-wind dynamics for spring, summer, autumn, and winter (*a*–*d*). The histograms under each panel show the number of individual measurements for a given time interval for nights with clouds (red shading) and without clouds (blue shading); the same colors are used for the main curves. The semi-transparent shading indicates the SD range of the component found. A similar representation for the meridional wind speed component is given in Figure 2.

Cloudiness has a noticeable effect on the measured wind speed values: on cloudy days they become closer to zero, whereas on clear days they have a much larger amplitude. As observed in Subsection 1.2, cloudiness leads to recording averaged signals with various Doppler shifts by the interferometer, which reduces the accuracy of calculating the wind speed.

Note also that the lack of measurements at certain points in time may be due not only to weather conditions, but also to possible technical reasons such as equipment maintenance periods.

HWM defines the wind speed at a given altitude, and the Fabry — Perot interferometer measures the emission intensity of the altitude layer, so the wind speed calculated from its measurements cannot be attributed to a specific altitude. The quantity obtained by the interferometer should be considered height-integrated. The emission intensity varies with height, and we can assume that the wind at different heights contributes variously to the height-integrated quantity. We have simulated the emission profile for several summer nights, which allowed us to identify the median profile (Figure 3), and have selected the most significant heights from 200 to 400 km at 50 km intervals [Tashchilin, Leonovich, 2016].

This profile allowed us to calculate weighting coefficients that take into account the emission contribution at different heights to the overall height-integrated quantity. Using these weighting coefficients, we calculated the equivalent height-integrated wind from HWM data.

2. RESULTS AND DISCUSSION

This section compares the horizontal-wind components obtained from the Fabry—Perot interferometer data: zonal U_{FPI} and meridional V_{FPI} with the corresponding values calculated by HWM93, HWM07, and HWM14 ($U_{93,07,14}$ and $V_{93,07,14}$). Figures 4 and 5 present averages of the equivalent height-integrated wind (blue line) and wind at a given height of 300 km (blue dots), which demonstrates both the most significant contribution of the latter to the integral and the overall correspondence of the diurnal variation of both series.

Subsections 2.1 and 2.2 analyze the zonal and meridional components respectively.

2.1. Zonal wind

During the initial comparison (see Figure 4), model and measured data shows similar features of the diurnal variation of the zonal wind. However, a more detailed examination reveals significant differences in amplitude and phase in each of the seasons at different time intervals.

In spring, there is the closest similarity in both curve shape and absolute values between U_{FPI} and U_{93} (panel *a*, red and blue colors respectively). This is especially evident in the time interval 13–20 UT: the difference between the model and the measurements in most cases does not exceed 20 m/s. In the latter part of the night, the discrepancies increase, but remain within the standard deviation (semi-transparent areas). The values of U_{07} (*b*) also coincide with measurements between 14 and 18 UT; however, after 18 UT there is both a significant discrepancy and a change of wind direction to westerly within the interval 18–22 UT. Comparison between U_{FPI} and U_{14}, on the contrary, demonstrates a closer correlation at the beginning and end of the night.

The summer period is characterized by the smallest number of measurements (histograms in panels *d*, *e*, *f*), which is associated with high cloudiness at this time of the year. The number of available values varies from 1 (minimum in the sample) to 12 (maximum for summer). For comparison, under ideal conditions up to 90 measurements could be made for 90 days, as, for example, in the case of the model. Thus, even the maximum number of measurements does not exceed 15 % of the possible. The lack of data also affects the width of the SD range: measurement fluctuations are practically not compensated by averaging. The histograms under each panel allow us to visually assess the reliability of the averaged values: the lower the bar, the less reliable the data. Considering this, a fairly correct comparison can be made only for the interval 14–18 UT. During this period, U_{14} and U_{93} show the best fit to U_{FPI}; whereas U_{07}, a significant discrepancy (to 60 m/s).

Autumn measurements (panels *g*, *h*, *i*) are more reliable due to a much larger amount of available data compared to spring and summer. This is probably what determines the best fit between U_{FPI} and U_{14} among all seasons: except for the last hour of the night, the discrepancy between them remains moderate (~25–30 m/s), and the curve shapes visually match well. The similarity is also observed for U_{93}, but in this case discrepancies arise not only at the end, but also at the beginning of the night. On the contrary, U_{07} demonstrates the largest discrepancy over the entire observation period. Values for the entire time interval are in antiphase: where the model predicts an easterly wind (positive values), the measurements are closer to zero or show negative values (wind in a westerly direction).

During the winter period (panels *j*, *k*, *l*), a similar dynamics is observed. Simulated U_{07} has values opposite to measured U_{FPI} except for a short time interval (~18:30–19:30 UT) during which the curves visually coincide, and the discrepancy does not exceed 20 m/s. The behavior of U_{14}, as in autumn, reproduces well the shape of the U_{FPI} curve for most of the interval except for the beginning and end of the night, where deviations occur. The U_{93} component also shows a profile similar to U_{FPI}, but there are discrepancies at the beginning and end of the night that are up to 40–60 m/s, which is much higher than for U_{14}.

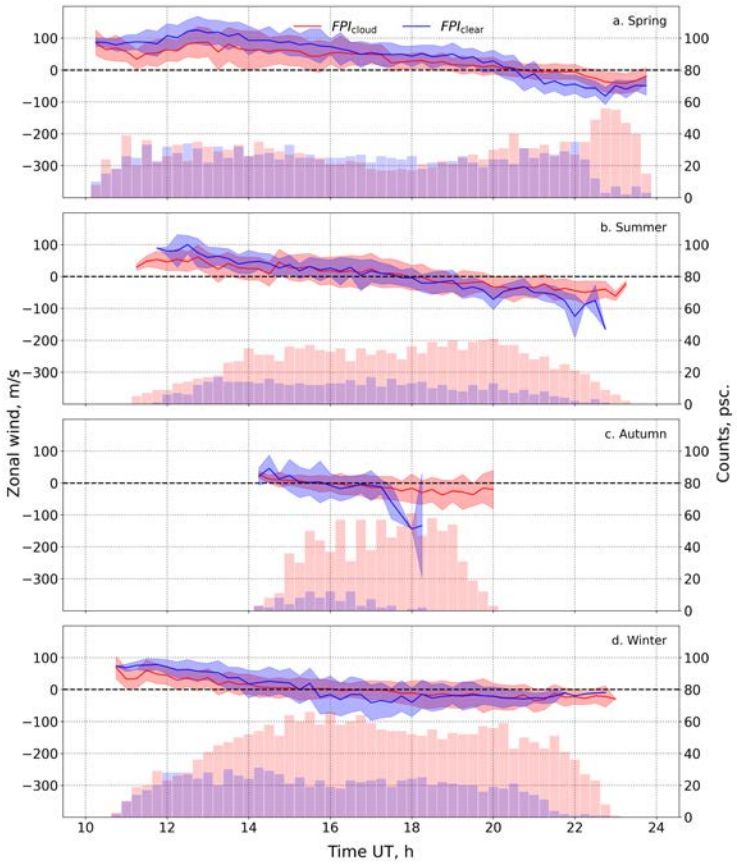

Figure 1. Comparison between cloudy-sky and clear-sky measurements; zonal component for spring, summer, autumn, and winter in 2022 (*a–d*)

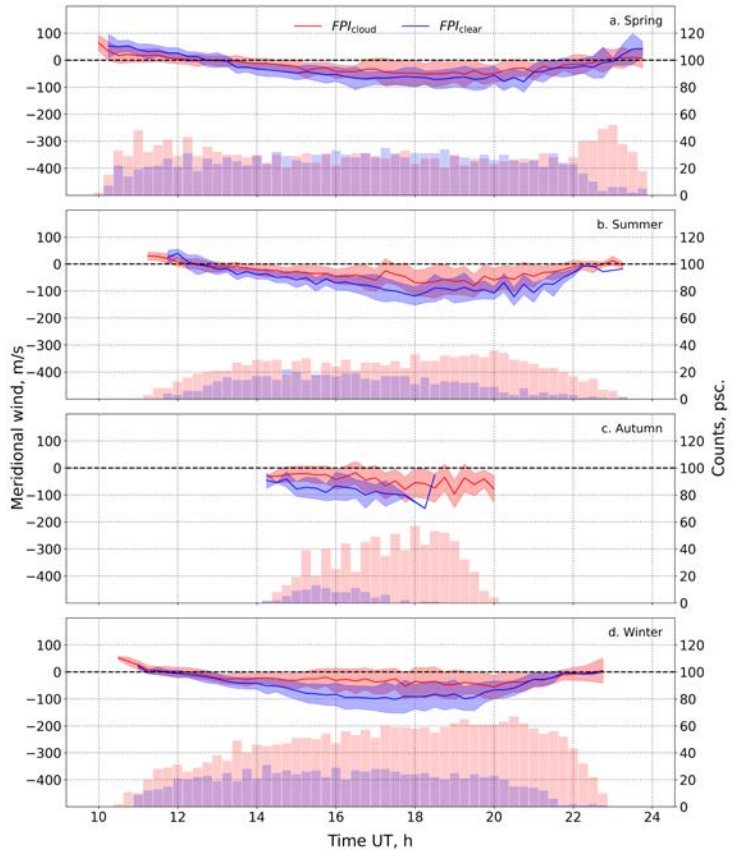

Figure 2. Comparison between cloudy-sky and clear-sky measurements; meridional component for spring, summer, autumn, and winter in 2022 (*a–d*)

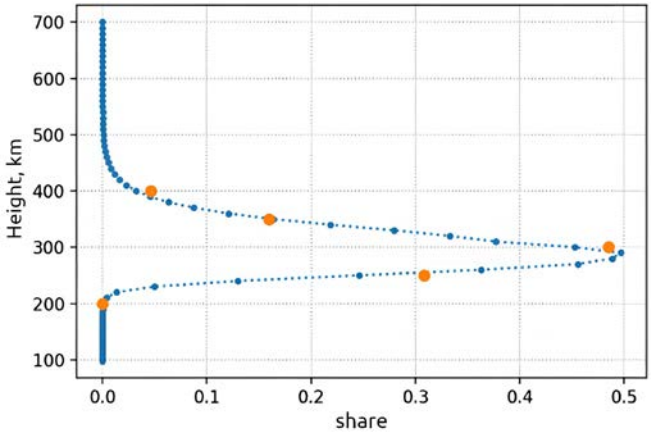

Figure 3. Normalized median height profile of the volume emission rate (blue) and the corresponding weighting coefficients (orange) at heights of 200, 250, 300, 350, and 400 km

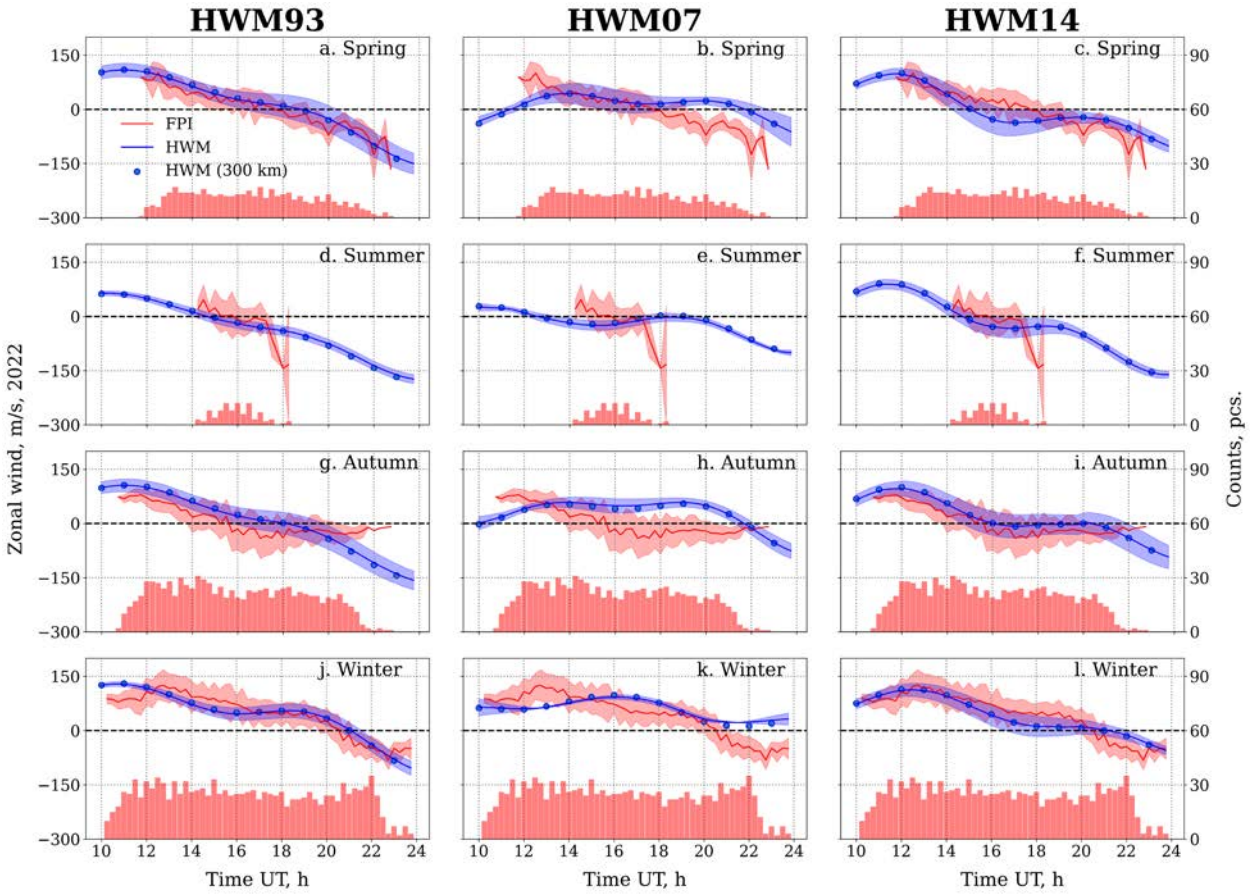

Figure 4. Zonal wind speed component. Red lines indicate interferometer measurements; blue lines, model values; dots mark averages of the wind component according to model data at a height of 300 km. Semi-transparent shading denotes the standard deviation (SD). From left to right — model versions (HWM93, HWM07, HWM14), from top to bottom — seasons (spring, summer, autumn, winter)

In general, the best fit between the zonal component and U_{FPI} measurements for all seasons is observed for HWM14, especially in autumn and winter. HWM93 commonly reproduces the general trend, but its values often differ from measurements at the beginning and end of the night. The largest deviations are typical of HWM07, and in a number of seasons the modeled values are in stable antiphase with measurements. Furthermore, regardless of the model version, larger discrepancies are systematically recorded at the boundaries of the observation interval at the beginning and end of the night.

2.2. Meridional wind

Figure 5 indicates that as in the case of the zonal wind speed component HWM reproduces the diurnal variation of the meridional wind. Moreover, despite the continuing discrepancies in amplitude and phase, the model and measured values of the meridional wind in most cases have the same direction.

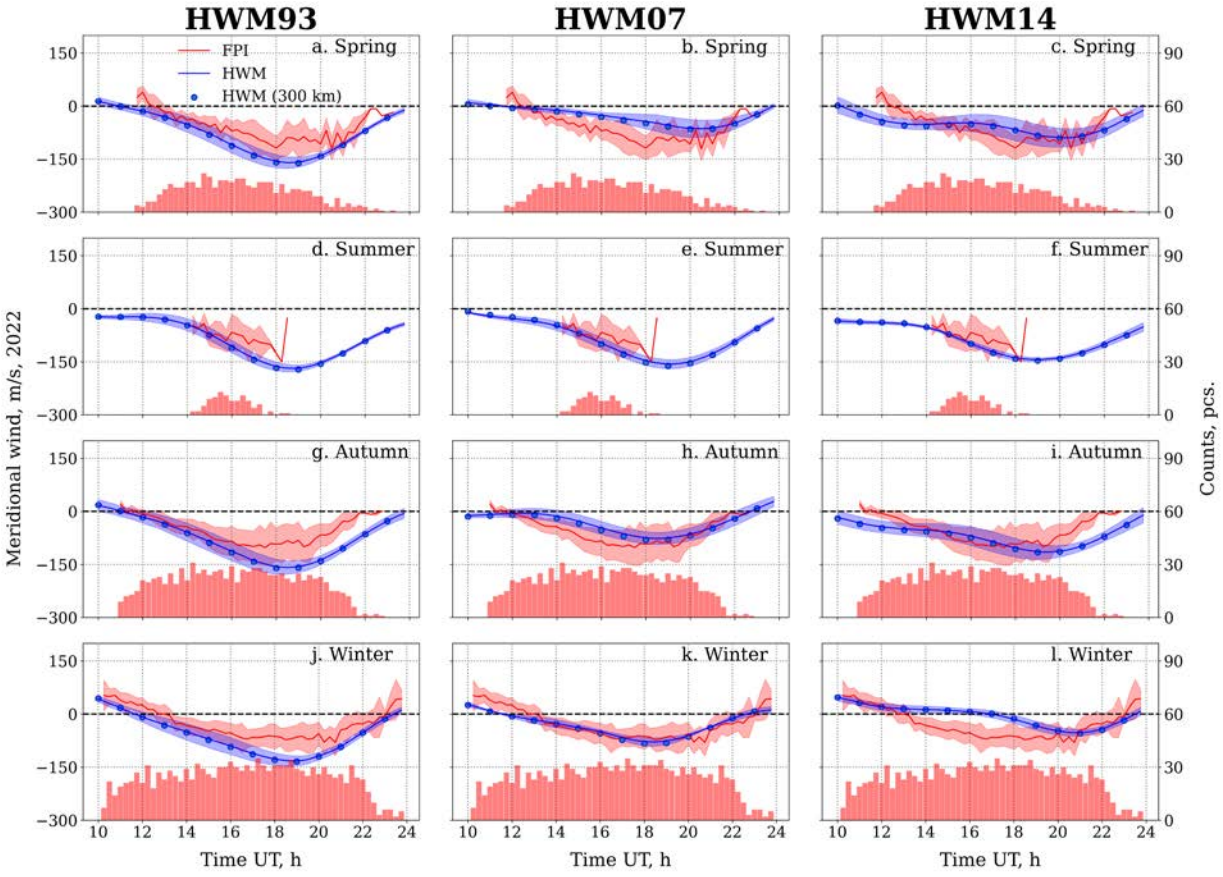

Figure 5. Meridional wind speed component. Red lines indicate interferometer measurements; blue lines, model values; dots mark averages of the wind component according to model data at a height of 300 km. Semi-transparent shading denotes the standard deviation (SD). The plots are arranged as follows: from left to right — model versions (HWM93, HWM07, HWM14), from top to bottom — seasons (spring, summer, autumn, winter)

In spring, V_{93} (panel *a*, blue) is most similar in shape to V_{FPI} (red), but the model values have a larger amplitude. On the contrary, V_{07} (*b*) is characterized by an underestimated amplitude compared to observations, as well as a time shift of the minimum toward the end of the night. In panel *c*, V_{14} has a curve shape similar to that of V_{FPI} and the smallest difference in amplitude within the interval 14–22 UT. In addition, there are deviations at the beginning and end of the night: to 30–70 m/s at 12–14 UT and to 30–50 m/s at 22–23 UT.

For summer, as in the case of the zonal component, the number of measurements (panels *d*, *e*, *f*, histograms) is significantly reduced after excluding cloudy nights. The observation interval at summer nights is limited in time and is ~5 hrs — from 14 to 19 UT. The maximum number of samples used in averaging does not exceed 13, hence individual outliers significantly distort the resulting values. In particular, from 18:00 to 18:30 UT there is a large discrepancy between the model and measured values (up to 140 m/s). We considered it necessary to retain such values in the plots, yet they have low statistical significance.

Autumn for all three versions of the model is characterized by a coincidence of the curve shape with that of V_{FPI} (panels *g*, *h*, *i*), while the minimum values in the model data are shifted in time relative to the measurements. For V_{93}, the amplitude of the discrepancies remains the largest, especially from midnight to the end of the night. V_{07} (*h*) demonstrates a good fit of the curve shape to that of V_{FPI} at minimum amplitude deviations as well. There is a correspondence between V_{14} (*i*) and V_{FPI} in the middle of the night, but at 11–14 and 20–23 UT discrepancies ~30–50 and 40–70 m/s, respectively, are recorded.

In winter, the V_{93} and V_{FPI} curves are also similar in shape (Figure 5, *j*), but in the range of minimum values the discrepancies are most pronounced: the model values have larger amplitudes. Panel *k* shows the closest agreement between model predictions of V_{07} and measurements of V_{FPI} for all seasons from midnight to the end of the night. At the same time, at the beginning of the night (10–13 UT), the discrepancies are as large as 40 m/s. On the contrary, V_{14} (*l*) demonstrates a good match with V_{FPI} at the beginning and end of the night, yet from 13 to 20 UT the values are in antiphase, and the discrepancies can be as large as 75 m/s.

For the meridional wind component, HWM07 is seen to fit interferometer measurements best of all, especially in autumn and winter. Unlike the zonal component for the meridional wind, model predictions more often agree with measurements, pronounced discrepancies at the beginning and end of the night are less common and have smaller amplitudes.

2.3. Discussion of discrepancies between measurements and model

After a detailed comparison between zonal and meridional wind speeds for all seasons, we can see that the discrepancy between model and measured values varies during the day for each season (Figures 6, 7). The red color indicates the discrepancy for the full set of measurements (cloudy and clear nights); blue, only for clear nights.

For the zonal wind component (see Figure 6) in almost all cases, the introduction of the cloudiness condition (ΔU_{clear}) does not significantly change the discrepancy between measured and model data. In some cases, it may even increase this discrepancy: in spring (*b*, *c*) and winter (*j*, *k*, *l*), at the end of the night; in autumn (*g*, *h*, *i*), at midnight. Probably, the difference between the full dataset and the data for clear nights is not so noticeable because cloudiness was recorded by a camera pointing north. This does not guarantee the presence or absence of clouds in other directions; therefore, such a data sample of cloud conditions has less effect on the zonal wind (west–east).

For the meridional component (north–south), the discrepancy between the model and observed values is more pronounced for the full dataset (ΔV_{all}) as compared to the dataset for clear nights (ΔV_{clear}). This is especially noticeable in summer for all three versions of the model (see Figure 7, *d*, *e*, *f*), as well as in spring, autumn, and winter for HWM93 (*a*, *g*, *l* respectively). In contrast, for autumn, HWM14 (*i*) shows a smaller discrepancy for the dataset for clear nights. However, at the same time, HWM07 for three seasons (*b*, *h*, *k*) and HWM14 for winter (*l*) clearly indicate in the sample for clear nights that the discrepancy between model data and measurements may increase.

In general, the discrepancies between measured and modeled meridional wind components are rather large for all seasons and all models. In some cases, for clear nights the meridional wind may have a discrepancy over 60 m/s; the zonal wind, over 120 m/s.

Tables 2 and 3 list mean discrepancies between measured and model data for each season for all models. The smallest discrepancies for a given season and model are highlighted in green. It is obvious that for the zonal wind the smallest discrepancy is observed by HWM14; and for the meridional wind, by HWM07. At the same time, this dependence persists both for the complete set of measurements and for the sample that includes only clear nights. Calculating the correlation between sets of averaged model and measured data is not very effective for the problem to solve, since it mainly reflects the behavior of variations and ignores the critically important wind strength and direction: a good correlation provides a similarity neither in direction nor in amplitude. This is clearly seen in data comparison in Tables 3 and 4. It is apparent that a high correlation does not guarantee a low discrepancy between measurements and the model: for example, V_{93} has the largest discrepancy (35 m/s) at 0.92 correlation. The cells demonstrating this contradiction are highlighted in red. We think that a good agreement is observed only for $U_{93spring}$ (green shading). Intermediate levels of the agreement are shown in yellow. Thus, we consider the data in Table 3 to be the most valuable part of the study.

Summarizing the data presented in Table 3, we can cautiously conclude that for the region of the Geophysical Observatory (Tory village), HWM14 (for the zonal wind component) and HWM07 (for the meridional one) show the best fit to observations. The low statistical significance of individual measurements and the limited consideration of the influence of the solar cycle phase must be taken into account: one-year observations cannot ensure the high reliability of conclusions.

The analysis has also revealed a number of factors contributing to discrepancies between model data and observations. First, it is the geographical limitation of the empirical base of the model: most ground-based measurements used in developing the HWM versions have been made mainly in the Western Hemisphere (North America, Europe). As a result, when employing the models in the Eastern Hemisphere (for example, in Eastern Siberia), systematic errors may occur, which is confirmed by the results of another study [Shcherbakov et al., 2015], where discrepancies between model predictions and observations were also detected. Secondly, unlike HWM93, HWM07 and HWM14 ignore the solar activity indices *F*10.7 and *F*10.7A [Drob et al., 2008, 2015]. As the developers of the model note, this limitation especially affects nighttime observations when there is no direct impact of solar radiation, but the accumulated effect of ultraviolet radiation remains which determines the global circulation in the thermosphere and hence the wind structure [Drob et al., 2008]. Given that our measurement data was obtained at night, the lack of consideration of solar activity parameters may be one of the causes of the systematic discrepancies identified in this study.

Note additionally that the discrepancies revealed in this study between the observed and model data on the neutral wind components are consistent with the results of similar foreign studies. For example, studies for mid-latitudes of China [Yao et al., 2015; Yang et al., 2020] also show that the HWM versions systematically underestimate or shift the amplitudes of night winds, and the agreement significantly depends on season and local time. When comparing interferometer observations with model data in East Asia [Jiang et al., 2018], phase shifts of the order of 1–3 hrs and regionally determined differences in zonal wind values similar to those obtained for the Baikal region were revealed. Similar features were observed at high latitudes in Norway: HWM14 correctly reproduced the overall dynamics, but showed significant differences in amplitude and phase [Xu et al., 2019]. Thus, our results agree with the conclusions drawn in foreign studies and confirm the presence of pronounced regional specificity in the operation of the HWM versions, especially at night and at latitudes for which the empirical database of the model is insufficient.

In the future, this research can be extended to several directions.

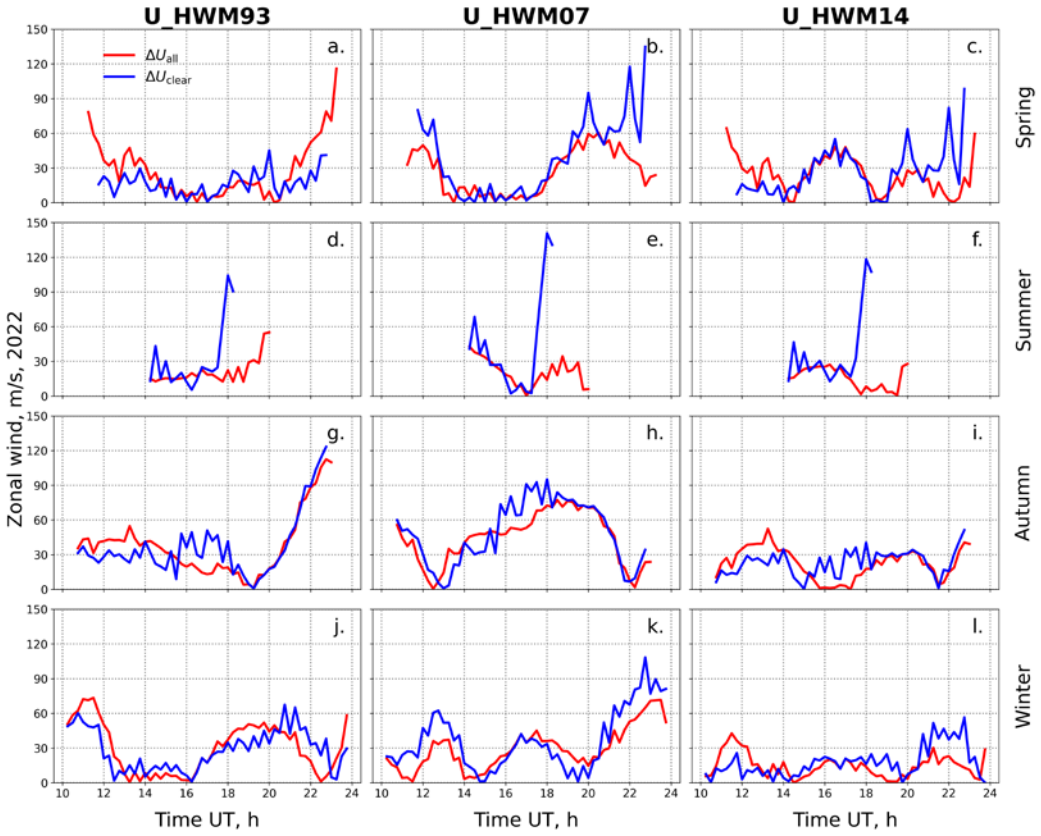

Figure 6. Modulus of the mean deviation of zonal components (measured and modeled). The red line ΔU_{all} represents the discrepancy between model and all measurements (including clear and cloudy nights); the blue line ΔU_{clear} indicates the discrepancy between the model and measurements made only at clear nights

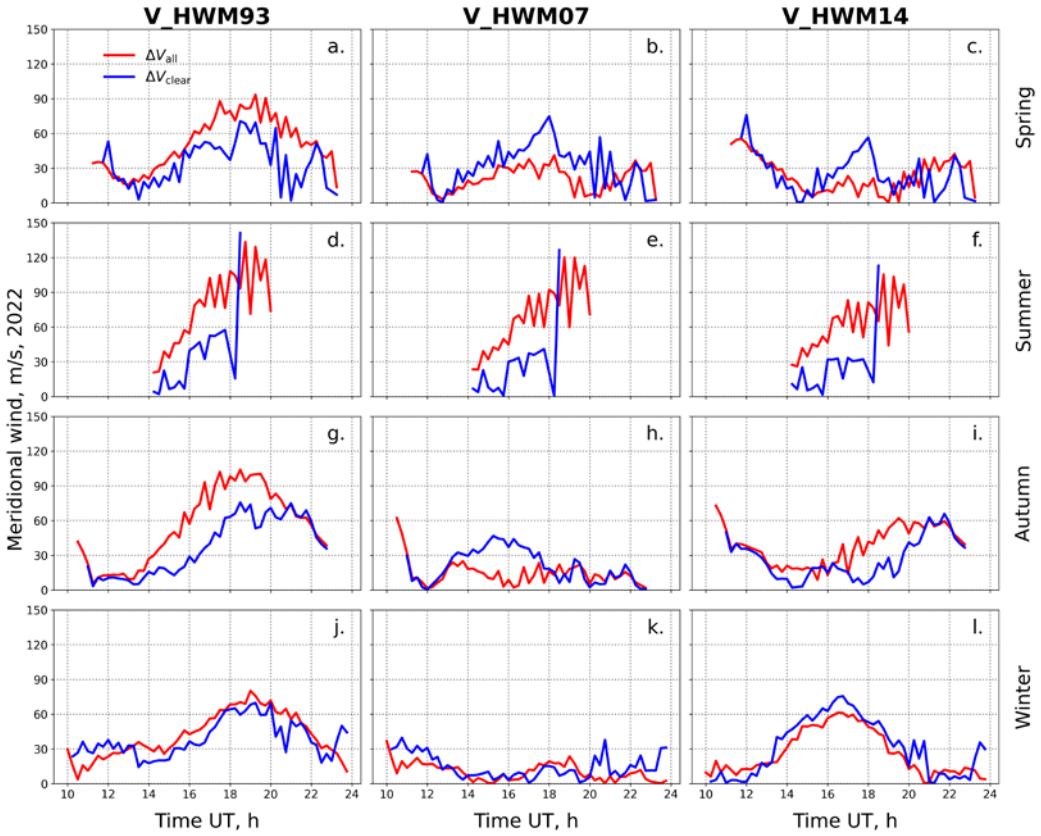

Figure 7. Modulus of the mean deviation of meridional components (measured and modeled). The red line ΔV_{all} denotes the discrepancy between model and all measurements (including clear and cloudy nights); the blue line ΔV_{clear}, the discrepancy between the model and measurements obtained only at clear nights

Table 2

Data for measurements excluding clouds

Wind	Model version	Nighttime average of discrepancy between measurements and model prediction, m/s				
		spring	summer	autumn	winter	year
zonal, *U*	HWM93	17	17	37	26	22
	HWM07	26	21	49	28	27
	HWM14	21	13	18	14	16
meridional, *V*	HWM93	50	78	56	36	53
	HWM07	21	65	12	9	16
	HWM14	22	61	42	19	32

Table 3

Data for measurements of clear nights

Wind	Model version	Nighttime average of discrepancy between measurements and model prediction, m/s				
		spring	summer	autumn	winter	year
zonal *U*	HWM93	16	21	30	28	24
	HWM07	35	27	51	31	33
	HWM14	21	20	21	16	20
meridional *V*	HWM93	35	27	35	34	53
	HWM07	31	20	19	11	16
	HWM14	22	21	23	30	32

Table 4

Correlation between datasets for clear nights

Wind	Model version	Coefficient of correlation with FPI data			
		spring	summer	autumn	winter
zonal *U*	HWM93	0.961	0.788	0.770	0.907
	HWM07	0.735	–0.836	0.023	0.762
	HWM14	0.814	0.474	0.901	0.912
meridional *V*	HWM93	0.927	0.495	0.889	0.962
	HWM07	0.744	0.482	0.844	0.917
	HWM14	0.684	0.495	0.668	0.620

- Extending the time range of observations to several years will increase the statistical significance of the results.
- Comparison of our measurement data with the results of observations from other observatories located in the Eastern Hemisphere (for example, in China). This could confirm or deny the existence of regional features of HWM.
- Given the importance of the influence of solar activity for night forecasts, we can recommend the de-

velopers of the model to include the *F*10.7 and *F*10.7A indices or try to develop our own model from HWM, which will take these indices into account.

Since models of different versions better describe different wind components, we can suggest using different versions of HWM depending on the season or problem being solved.

CONCLUSIONS

This paper has compared the horizontal wind components obtained from the Fabry—Perot interferometer data with the results of the empirical model HWM of three versions (HWM93, HWM07, HWM14). The comparison was carried out separately for the zonal and meridional components, taking into account seasons and the influence of observational conditions (cloudiness).

The results have shown the following.

- For the zonal wind component, HWM14 demonstrates the best fit to the measurements, especially in autumn and winter.
- For the meridional component, the values closest to the measurements are given by HWM07. In most cases, wind directions accord with the measurements.
- In all seasons, the greatest discrepancies between the model and measured data are generally observed at the beginning and end of the night.
- The presence of clouds can affect the reliability of the data obtained by the interferometer, underestimating the amplitudes of the measured wind.

A number of factors may explain the discrepancies between the model and measured values. In particular, HWM07 and HWM14 ignore the solar activity indices *F*10.7 and *F*10.7A, unlike HWM93, which may explain its best results in some cases.

In addition, HWM is based primarily on data from instruments located in the Western Hemisphere, whereas the measurements used in this work were obtained by the Fabry—Perot interferometer in the Eastern Hemisphere (Tory village, Republic of Buryatia). This explains the decrease in model accuracy in these regions.

The findings can be used to refine the conditions of applicability of HWM.

The results were obtained using the Large-Scale Research Facility “Optical Instruments” of ISTP SB RAS [https://ckp-rf.r u/catalog/usu/4138180/]. The work was financially supported by the Ministry of Science and Higher Education of the Russian Federation (Grant No. 075-GZ/C3569/278).

REFERENCES

Drob D.P. et al. An empirical model of the Earth’s horizontal wind fields: HWM07. *J. Geophys. Res.: Space Phys.* 2008, vol. 113, iss. A12. https://doi.org/10.1029/2008JA013668.

Drob D.P. et al. An update to the Horizontal Wind Model (HWM): The quiet time thermosphere. *Earth and Space Sci.* 2015, vol. 2, pp. 301–319. https://doi.org/10.1002/2014EA000089.

Emmert J.T. et al. Climatologies of nighttime upper thermospheric winds measured by ground-based Fabry—Perot interferometers during geomagnetically quiet conditions: 1. Local time, latitudinal, seasonal, and solar cycle dependence. *J. Geophys. Res.: Space Phys.* 2006, vol. 111, iss. A12. https://doi.org/10.1029/2006JA011948.

Fuller-Rowell T.J. et al. *A Coupled Thermosphere–Ionosphere Model (CTIM)*. In: Schunk R.W. (ed.) Solar-Terrestrial Energy Program: Handbook of Ionospheric Models. Logan, Utah State Univ. Press. 1996, pp. 217–238.

Hedin A.E. et al. Empirical global model of upper thermosphere winds based on Atmosphere and Dynamics Explorer satellite data. *J. Geophys. Res.: Space Phys.* 1988, vol. 93, iss. A9, pp. 9959–9978. https://doi.org/10.1029/JA093iA09p09959.

Hedin A.E. et al. Revised global model of thermosphere winds using satellite and ground-based observations. *J. Geophys. Res.: Space Phys.* 1991, vol. 96, iss. A5, pp. 7657–7688. https://doi.org/10.1029/91JA00251.

Hedin A.E. et al. Empirical wind model for the upper, middle and lower atmosphere. *J. Atmos. Solar-Terr. Phys.* 1996, vol. 58, iss. 13, pp. 1421–1447. https://doi.org/10.1016/0021-9169(95)00122-0.

Holton J.R., Hakim G.J. *An Introduction to Dynamic Meteorology*. Academic Press, 2012, 532 p.

Jiang G., Xu J., et al. A comparison of quiet-time thermospheric winds between FPI observations and model calculations. *J. Geophys. Res.: Space Phys.* 2018, vol. 123, pp. 7789–7805. https://doi.org/10.1029/2018JA025424.

Klimenko M.V. et al. Numerical modeling of the equatorial electrojet UT-variation on the basis of the model GSM TIP. *Adv. Radio Sci.* 2007, vol. 5, pp. 385–392. https://doi.org/10.5194/ars-5-385-2007.

Matveev L.T. *Course of General Meteorology. Physics of the Atmosphere.* Leningrad, Gidrometeoizdat Publ., 1984, 752 p. (In Russian).

Okoh D. et al. Thermospheric neutral wind measurements and investigations across the African region — A review. *Atmosphere*. 2022, vol. 13, no. 6, p. 863. https://doi.org/10.3390/atmos13060863.

Podlesnyi S.V. et al. Comparing methods to estimate cloud cover over the Baikal natural territory in December 2020. *Sol.-Terr. Phys*. 2022, vol. 8, iss. 4, pp. 95–102. https://doi.org/10.12737/stp-84202210.

Prölss G. Physics of the Earth’s Space Environment: An Introduction. Springer. 2012, 486 p.

Richmond A.D., Maute A. Ionospheric electrodynamics modeling. In: Modeling the Ionosphere—Thermosphere System. Wiley, 2014, pp. 57–71.

Richmond A.D. et al. A thermosphere/ionosphere general circulation model with coupled electrodynamics. *Geophys. Res. Lett.* 1992, vol. 19, iss. 6, pp. 601–604. https://doi.org/10.1029/92GL00401.

Ridley A.J. et al. The global ionosphere–thermosphere model. J. *Atmos. Solar–Terr. Phys.* 2006, vol. 68, pp. 839–864. https://doi.org/10.1016/j.jastp.2006.01.008.

Shcherbakov A.A. et al. Calculation of neutral meridional winds at midlatitudes using the Irkutsk Incoherent Scatter Radar. *Solnechno-zemnaya fizika* [Solar-Terr. Phys.]. 2015, vol. 1, iss. 3, pp. 37–48. https://doi.org/10.12737/10962. (In Russian).

Tashchilin A.V., Leonovich L.A. Modeling nightglow in atomic oxygen red and green lines under moderate disturbed geomagnetic conditions at midlatitudes. *Sol.-Terr. Phys*. 2016, vol. 2, iss. 4, pp. 94–106. https://doi.org/10.12737/24276.

Vasiliev R.V. et al. Registration of upper atmosphere parameters in Eastern Siberia using the Fabry—Perot interferometer KEO Scientific “Arinae”. *Sol.-Terr. Phys*. 2017, vol. 3, iss. 3, pp. 61–75. https://doi.org/10.12737/stp-33201707.

Vasiliev R.V. et al. Scientific goals of optical instruments of the National Heliogeophysical Complex. *Sol.-Terr. Phys*. 2020, vol. 6, iss. 2, pp. 84–97. https://doi.org/10.12737/stp-62202008.

Xu H. et al. High-latitude thermospheric wind study using a Fabry—Perot interferometer at Tromsø in Norway: averages and variations during quiet times. *Earth, Planets and Space*. 2019, vol. 71, article 110. https://doi.org/10.1186/s40623-019-1093-8.

Yang C. et al. Climatology of nighttime upper thermospheric winds from Fabry—Perot interferometer 2011–2019 measurements over Kelan (38.7 N, 111.6 E), China: Local time, seasonal, solar cycle, and geomagnetic activity dependence. *J. Geophys. Res.: Space Phys.* 2020, vol. 125, iss 9, e2020JA027892. https://doi.org/10.1029/2020JA027892.

Yao X. et al. Climatological modeling of horizontal winds in the mesosphere and lower thermosphere over a mid-latitude station in China. *Adv. Space Res.* 2015, vol. 56, iss. 7, pp. 1354–1365. https://doi.org/10.1016/j.asr.2015.06.026.

Zherebtsov G.A.. Complex of heliogeophysical instruments of new generation. *Sol.-Terr. Phys.* 2020, vol. 6, iss. 2, pp. 3–13. https://doi.org/10.12737/stp-62202001.

URL: https://ccmc.gsfc.nasa.gov/models/HWM14~2014/ (accessed February 27, 2026).

URL: https://nom.esa.int/models/hwm (accessed February 27, 2026).

URL: https://github.com/timduly4/pyglow (accessed February 27, 2026).

URL: https://ckp-rf.ru/catalog/usu/4138180/ (accessed February 27, 2026).

Original Russian version: Budovkina A.A. et al., published in Solnechno-zemnaya fizika. 2026, vol. 12, no. 2, pp. 63–75. https://doi.org/10.12737/szf-122202607.

How to cite this article

Budovkina A.A. et al. Seasonal variability of horizontal neutral wind in the Baikal region from Fabry—Perot interferometer observations and different versions of the HWM model. *Sol.-Terr. Phys*. 2026, vol. 12, iss. 2, pp. 57–68. https://doi.org/10.12737/stp-122202607.